Micro-earthquake monitoring with sparsely-sampled data

Paul Sava, Center for Wave Phenomena, Colorado School of Mines

SUMMARY

Micro-seismicity can be used to monitor the migration of fluids during reservoir production and hydro-fracturing operations in brittle formations or for studies of naturally occurring earthquakes in fault zones. Micro-earthquake locations can be inferred using wave-equation imaging under the exploding reflector model, assuming densely sampled data and known velocity. Seismicity is usually monitored with sparse networks of seismic sensors, for example located in boreholes. The sparsity of the sensor network itself degrades the accuracy of the estimated locations, even when the velocity model is accurately known, thus limiting the resolution at which fluid pathways can be inferred. Wavefields reconstructed in known velocity using data recorded with sparse arrays can be described as having a random character due to the incomplete interference of wave components. Similarly, wavefields reconstructed in unknown velocity using data recorded with dense arrays can be described as having a random character due to the inconsistent interference of wave components. In both cases, the reconstructed wavefields are characterized by random fluctuations which obstruct focusing that occurs at source locations. This situation can be improved using interferometry in the imaging process. Reverse-time imaging with an interferometric imaging condition attenuates random fluctuations, thus producing crisper images which support the process of robust automatic micro-earthquake location. The similarity of random wavefield fluctuations due to model fluctuations and sparse acquisition, as well as the applicability of conventional and interferometric imaging techniques, are illustrated in this paper with a complex synthetic example.

INTRODUCTION

Seismic imaging based on the single scattering assumption, also known as Born approximation, consists of two main steps: *wavefield reconstruction* which serves the purpose of propagating recorded data from the acquisition surface back into the subsurface, followed by an *imaging condition* which serves the purpose of highlighting locations where scattering occurs. This framework holds both when the source of seismic waves is located in the subsurface and the imaging target consists of locating this source, as well as when the source of seismic waves is located on the acquisition surface and the imaging target consists of locating the places in the subsurface where scattering or reflection occurs. In this paper, I concentrate on the case of imaging seismic sources located in the subsurface, although the methodology discussed here applies equally well for the more conventional imaging with artificial sources.

An example of seismic source located in the subsurface is represented by micro-earthquakes triggered by natural causes or by fluid injection during reservoir production or fracturing. One application of micro-earthquake location is monitoring of fluid injection in brittle reservoirs when micro-earthquake evolution in time correlates with fluid movement in reservoir formations. Micro-earthquakes can be located using several methods including double-difference algorithms (Waldhauser and Ellsworth, 2000), Gaussian-beam migration (Rentsch et al., 2004), diffraction stacking (Gajewski et al., 2007) or reverse-time migration (Gajewski and Tessmer, 2005; Vasconcelos et al., 2007).

Micro-earthquake location using reverse-time migration, which is the technique advocated in this paper, follows the same general pattern mentioned in the preceding paragraph: wavefield-reconstruction backward in time followed by an imaging condition extracting the image, i.e. the location of the source. The main difficulty with this procedure is that the onset of the micro-earthquake is unknown, i.e. time $t = 0$ is unknown, so the imaging condition cannot be simply applied as it is usually done in zero-offset migration. Instead, an automatic search needs to be performed in the back-propagated wavefield to identify the locations where wavefield energy focuses. This process is difficult and often ambiguous since false focusing locations might overlap with locations of wavefield focusing. This is particularly true when imaging using an approximate model which does not explain all random fluctuations observed in the recorded data. This problem is further complicated if the acquisition array is sparse, e.g. when receivers are located in a borehole. In this case, the sparsity of the array itself leads to artifacts in the reconstructed wavefield which makes the automatic picking of focused events even harder.

The process by which sampling artifacts are generated is explained in Figures 1(a)-1(c). Each segment in Figure 1(a) corresponds to a wavefront reconstructed from a receiver. For dense and uniform receiver coverage and reconstruction using accurate velocity, the wavefronts overlap at the source position. However, if the velocity for wavefield reconstruction is inaccurate, then the wavefronts do not all overlap at the source position, Figure 1(b), thus leading to imaging artifacts. Likewise, if receiver sampling is sparse, reconstruction at the source position is incomplete, Figure 1(c), even if the velocity used for reconstruction is accurate. The cartoons depicted in Figures 1(a)-1(c) represent an ideal situation with receivers surrounding the seismic source, which is not typical for seismic experiments. In those cases, source illumination is limited to a range which correlates with the receiver coordinates.
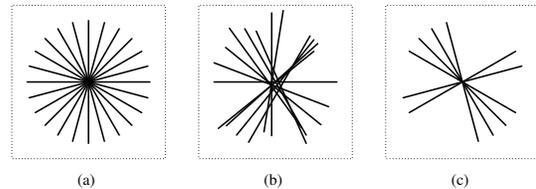

Figure 1: Schematic representation of point source reconstruction in various imaging scenarios: (a) using known velocity and uniformly sampled data at locations surrounding the source, (b) using unknown velocity and uniformly sampled data and (c) using known velocity and non-uniformly sampled data. Each segment represents a portion of a wavefront reconstructed at the location of the source from a given receiver.

In general, artifacts caused by unknown velocity fluctuations and receiver sampling overlap and, although the two phenomena are not equivalent, their effect on the reconstructed wavefields are analogous. As illustrated in the following sections, the general character of those artifacts is that of random wavefield fluctuations. Ideally, the imaging procedure should attenuate random wavefield fluctuations irrespective of their cause in order to support automatic source identification.

CONVENTIONAL IMAGING CONDITION

Assuming data $D(\mathbf{x},t)$ acquired at coordinates $\mathbf{x}$ function of time t (e.g. in a borehole) we can reconstruct the wavefield $V(\mathbf{x},\mathbf{y},t)$ at coordinates $\mathbf{y}$ in the imaging volume using an appropriate Green's function $G(\mathbf{x},\mathbf{y},t)$ corresponding to the locations $\mathbf{x}$ and $\mathbf{y}$ (Figure 2)

$$V(\mathbf{x},\mathbf{y},t) = D(\mathbf{x},t) *_t G(\mathbf{x},\mathbf{y},t) , \qquad (1)$$

where the symbol $*_t$ indicates time convolution. The total wavefield $U(\mathbf{y},t)$ at coordinates $\mathbf{y}$ due to data recorded at all receivers located at coordinates $\mathbf{x}$ is represented by the superposition of the reconstructed wavefields $V(\mathbf{x},\mathbf{y},t)$:

$$U(\mathbf{y},t) = \int_{\mathbf{x}} d\mathbf{x}\, V(\mathbf{x},\mathbf{y},t) \; . \tag{2}$$

A conventional imaging condition (CIC) applied to this reconstructed wavefield extracts the image $R_{CIC}(\mathbf{y})$ as the wavefield at time $t=0$

$$R_{CIC}(\mathbf{y}) = U(\mathbf{y},t=0) \; . \tag{3}$$

This imaging procedure succeeds if several assumptions are fulfilled: first, the velocity model used for imaging has to be accurate; second, the numeric solution to the wave-equation used for wavefield reconstruction has to be accurate; third, the data need to be sampled densely and uniformly on the acquisition surface. Here, I assume that the first and third assumptions are not fulfilled. In these cases, the imaging is not accurate because contributions to the reconstructed wavefield from the receiver coordinates do not interfere constructively, thus leading to imaging artifacts. As indicated earlier, this situation is analogous to the case of imaging with an inaccurate velocity model, e.g. imaging with a smooth velocity of data corresponding to geology characterized by rapid velocity variations.
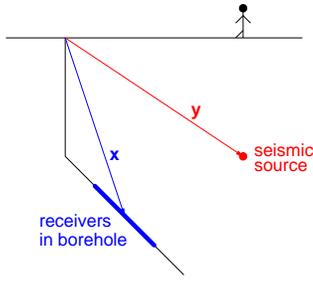

Figure 2: Illustration of the variables $\mathbf{x}$ and $\mathbf{y}$ used in text for the description of the conventional and interferometric imaging procedures.

Different image processing procedures can be employed to reduce the random wavefield fluctuations. The procedure advocated in this paper uses interferometry for noise cancellation. Interferometric procedures can be formulated in various frameworks, e.g. coherent interferometric imaging (Borcea et al., 2006) or wave-equation migration with an interferometric imaging condition (Sava and Poliannikov, 2008).

INTERFEROMETRIC IMAGING CONDITION

Migration with an interferometric imaging condition (IIC) uses the same generic framework as the one used for the conventional imaging condition, i.e. wavefield reconstruction followed by an imaging condition. However, the difference is that the imaging condition is not applied to the reconstructed wavefield directly, but it is applied to the wavefield which has been transformed using pseudo Wigner distribution functions (WDF) (Wigner, 1932). By definition, the zero frequency pseudo WDF of the reconstructed wavefield $U(\mathbf{y},t)$ is

$$W(\mathbf{y},t) = \int\limits_{|t_h|\leq T} dt_h \int\limits_{|\mathbf{y}_h|\leq Y} d\mathbf{y}_h\, U\left(\mathbf{y}-\frac{\mathbf{y}_h}{2},t-\frac{t_h}{2}\right) U\left(\mathbf{y}+\frac{\mathbf{y}_h}{2},t+\frac{t_h}{2}\right) ,$$
$$\tag{4}$$

where Y and T denote averaging windows in space and time, respectively. In general, Y is three dimensional and T is one dimensional.

Then, the image $R_{IIC}(\mathbf{y})$ is obtained by extracting the time $t=0$ from the pseudo WDF, $W(\mathbf{y},t)$, of the wavefield $U(\mathbf{y},t)$:

$$R_{IIC}(\mathbf{y}) = W(\mathbf{y},t=0) \; . \tag{5}$$

The interferometric imaging condition represented by equations 4 and 5 effectively reduces the artifacts caused by the random fluctuations in the wavefield by filtering out its rapidly varying components (Sava and Poliannikov, 2008). In this paper, I use this imaging condition to attenuate noise caused by sparse data sampling or noise caused by random velocity variations. As suggested earlier, the interferometric imaging condition attenuates both types of noise at once, since it does not explicitly distinguish between the various causes of random fluctuations.

The parameters Y and T defining the local window of the pseudo WDF are selected according to two criteria (Cohen, 1995). First, the windows have to be large to enclose a representative portion of the wavefield which captures the random fluctuation of the wavefield. Second, the window has to be small to limit the possibility of cross-talk between various events present in the wavefield. Furthermore, cross-talk can be attenuated by selecting windows with different shapes, for example Gaussian or exponentially-decaying. For simplicity, in all examples presented in this paper, the space and time windows are rectangular with no tapering and the size is selected assuming that micro-earthquakes occur sufficiently sparse, i.e. the various sources are located at least twice as far in space and time relative to the wavenumber and frequency of the considered seismic event. The windows used here are 11 grid points in space and 5 grid points in time.

EXAMPLE

I exemplify the interferometric imaging condition method with a synthetic example simulating the acquisition geometry of the passive seismic experiment performed at the San Andreas Fault Observatory at Depth (Chavarria et al., 2003). This numeric experiment simulates waves propagating from three micro-earthquake sources located in the fault zone, Figure 3, which are recorded in a deviated well located at a distance from the fault. For the imaging procedure described in this paper, the micro-earthquakes represent the seismic sources. This experiment uses acoustic waves, corresponding to the situation in which we use the P-wave mode recorded by the three-component receivers located in the borehole, Figures 4(b) and 5(b). The three sources are triggered 40 ms apart and the triggering time of the second source is conventionally taken to represent the origin of the time axis.
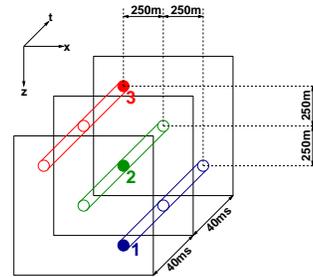

Figure 3: Geometry of the sources used in the numeric experiment. The horizontal and vertical separation between sources is 250 m. The sources are triggered with 40 ms delays in the order indicated by their numbers. Time $t=0$ is conventionally set to the the triggering moment of source 2.

The goal of this experiment is to locate the source positions by focusing data recorded using dense acquisition in media with random fluctuations or by focusing data recorded using sparse acquisition arrays
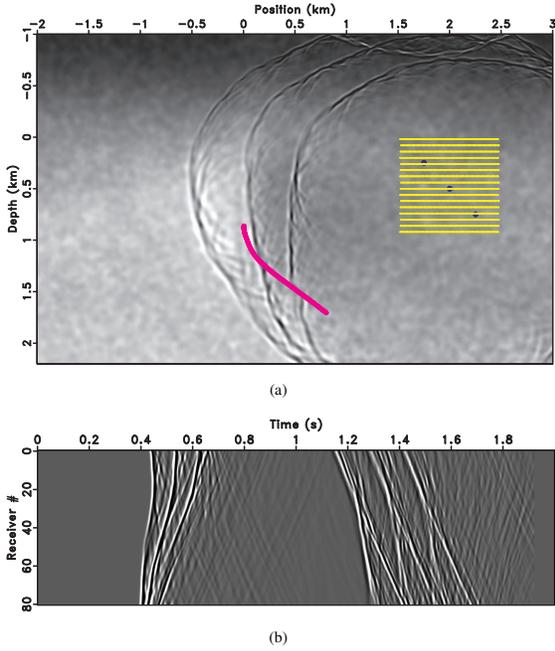
Figure 4: (a) Wavefields simulated in random media and (b) data acquired with a dense receiver array. Overlain on the model and wavefield are the positions of the sources and borehole receivers. The hashed area corresponds to the images depicted in Figures 6(a)-6(b).
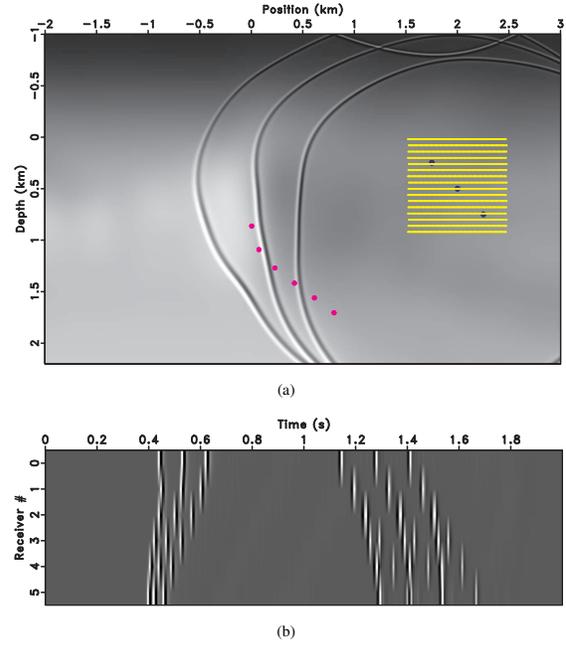

Figure 5: (a) Wavefields simulated in smooth media and (b) data acquired with a sparse receiver array. Overlain on the model and wavefield are the positions of the sources and borehole receivers. The hashed area corresponds to the images depicted in Figures 7(a)-7(b).

in media without random fluctuations. In the first case, the imaging artifacts are caused by the fact that data are imaged with a velocity model that does not incorporate all random fluctuations of the model used for data simulation, while in the second case, the imaging artifacts are caused by the fact that the data are sampled sparsely in the borehole array.

Figures 6(a)-6(b) and 7(a)-7(b) show the wavefields reconstructed in reverse time around the target location. From left to right, the panels represent the wavefield at different times. As indicated earlier, the time at which source 2 focuses is selected as time $t = 0$, although this convention is not relevant for the experiment and any other time could be selected as reference. The experiment depicted in Figures 6(a)-6(b) corresponds to modeling in a model with random fluctuations and migration in a smooth background model. In this experiment, the data used for imaging are densely-sampled in the borehole. In contrast, the experiment depicted in 7(a)-7(b) corresponds to modeling and migration in the smooth background model. In this experiment, the data are sparsely-sampled in the borehole. In both cases, panels (a) correspond to imaging with a conventional imaging condition (CIC), i.e. simply select the reconstructed wavefield at various times, and panels (b) correspond to imaging with the interferometric imaging condition, i.e. select various times from the wavefield transformed with a pseudo-WDF of 11 grid points in space and 5 grid points in time. For this example, WDF window corresponds to 44 m in space and 2 ms in time.

Figure 6(a) shows significant random fluctuations caused by wavefield reconstruction using an inaccurate velocity model. The fluctuations caused by the random velocity and encoded in the recorded data are not corrected during wavefield reconstruction and they remain present in the model. Likewise, Figure 7(a) shows significant random fluctuations caused by reconstruction using the sparse borehole data. However, the zero-frequency pseudo WDF applied to the reconstructed wavefields attenuates the rapid wavefield fluctuations and leads to sparser, better focused images that are easier to use for source

location. This conclusion applies equally well for the experiments depicted in Figures 6(a)-6(b) or 7(a)-7(b).

Finally, I note that the 2D imaging results from this example show better focusing than what would be expected in 3D. This is simply because the 1D acquisition in the borehole cannot constrain the 3D location of the micro-earthquakes, i.e. the azimuthal resolution is poor, especially if scatterers are not present in the model used for imaging. This situation can be improved by using data acquired in several boreholes or by using additional information extracted from the wavefields, e.g. polarization of multicomponent data.

CONCLUSIONS

The interferometric imaging condition used in conjunction with reverse-time migration reduces the artifacts caused by random velocity fluctuations that are unaccounted-for in imaging and by the sparse wavefield sampling on the acquisition array. The images produced by this procedure are crisper and support automatic picking of micro-earthquake locations. The interferometric imaging procedure has a similar structure to conventional imaging and the moderate cost increase is proportional to the size of the windows used by the pseudo Wigner distribution functions. The source positions obtained using this procedure can be used to monitor fluid injection or for studies of naturally occurring earthquakes in fault zones.

ACKNOWLEDGMENT
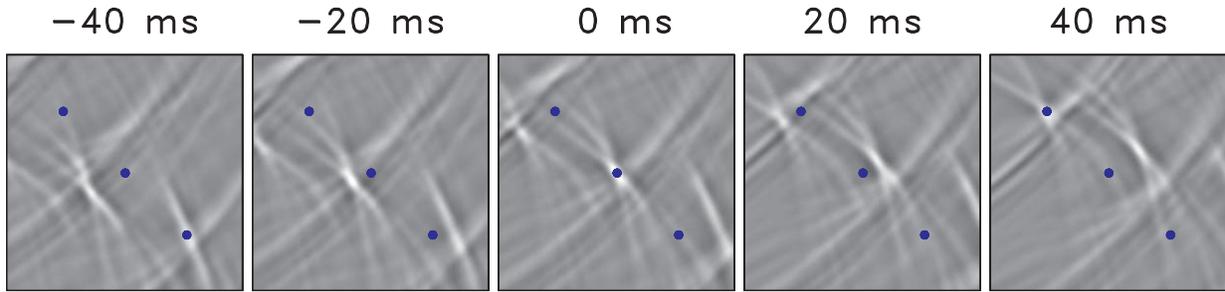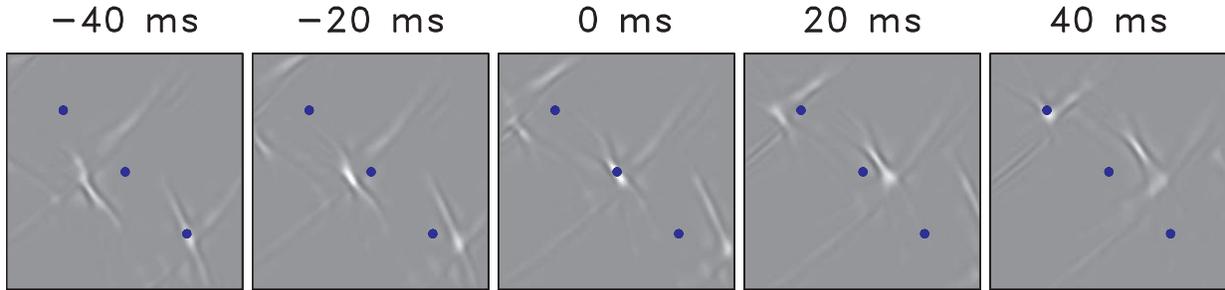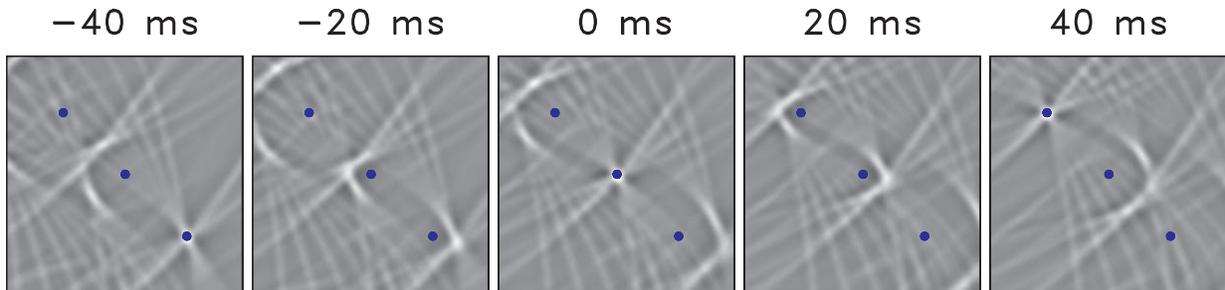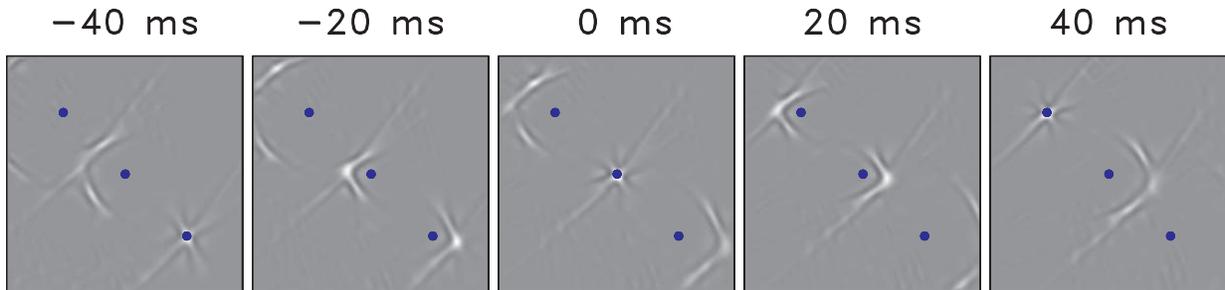
Figure 6: Images corresponding to migration of the *densely-sampled data* modeled in the *random velocity* by (a) conventional I.C. and (b) interferometric I.C. using the background velocity. The left-most panel shows focusing at source 1, the middle panel shows focusing at source 2, and the right-most panel shows focusing at source 3. The overlain dots represent the exact source positions.

Figure 7: Images corresponding to migration of the *sparsely-sampled data* modeled in the *background velocity* by (a) conventional I.C. and (b) interferometric I.C. using the background velocity. The left-most panel shows focusing at source 1, the middle panel shows focusing at source 2, and the right-most panel shows focusing at source 3. The overlain dots represent the exact source positions.

REFERENCES

Borcea, L., G. Papanicolaou, and C. Tsogka, 2006, Coherent interferometric imaging in clutter: Geopysics, **71**, SI165–SI175.

Chavarria, J., P. Malin, E. Shalev, and R. Catchings, 2003, A look inside the San Andreas Fault at Parkfield through Vertical Seismic Profiling: Science, **302**, 1746–1748.

Cohen, L., 1995, Time Frequency Analysis: Prentice Hall Signal Processing Series.

Gajewski, D., D. Anikiev, B. Kashtan, E. Tessmer, and C. Vanelle, 2007, Localization of seismic events by diffraction stacking: 76th Annual International Meeting, SEG, Expanded Abstracts, 1287–1291.

Gajewski, D. and E. Tessmer, 2005, Reverse modelling for seismic event characterization: Geophysical Journal International, **163**, 276–284.

Rentsch, S., S. Buske, S. Luth, and S. A. Shapiro, 2004, Location of seismicity using Gaussian beam type migration: 74th Ann. Internat. Mtg., 354–357, Soc. of Expl. Geophys.

Sava, P. and O. Poliannikov, 2008, Interferometric imaging condition for wave-equation migration: Geophysics, **73**, S47–S61.

Vasconcelos, I., S. Taylor, R. Snieder, A. Chavarria, P. Sava, and P. Malin, 2007, Broadside interferometric and reverse-time imaging of the San Andreas fault at depth: 77th Annual International Meeting, SEG, Expanded Abstracts, 2175–2178.

Waldhauser, F. and W. Ellsworth, 2000, A double-difference earthquake location algorithm: Method and application to the northern Hayward fault: Bulletin of the Seismological Society of America, **90**, 1353–1368.

Wigner, E., 1932, On the quantum correction for thermodynamic equilibrium: Physical Review, **40**, 749–759.